Current Biology

Report

Hypothalamic tanycytes as mediators of maternally programmed seasonal plasticity

Graphical abstract

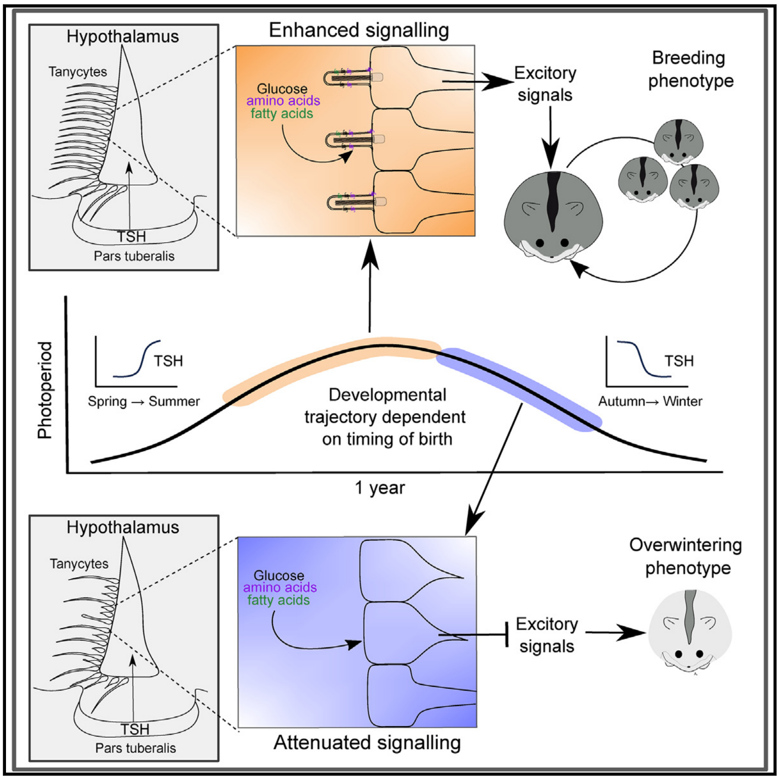

Authors

Vebjørn J. Melum,
Cristina Sáenz de Miera,
Fredrik A.F. Markussen, ...,
Valérie Simonneaux,
David G. Hazlerigg, Shona H. Wood

Correspondence

david.hazlerigg@uit.no (D.G.H.),
shona.wood@uit.no (S.H.W.)

In brief

Hypothalamic tanycytes are glial cells implicated in hypothalamic sensing of metabolic status. Melum et al. show that, in Siberian hamsters, tanycyte sensory attributes are highly sensitive to early life programming by light exposure *in utero* and post-natally. A model linking this phenomenon to seasonal programming of life history is proposed.

Highlights

- Siberian hamster development depends on pre- and post-natal photoperiod experience
- Tanycyte transcriptome is highly photoperiod sensitive
- Tanycytes have fewer sensory cilia in short photoperiod-raised hamsters
- Increasing photoperiod post-weaning stimulates ciliogenesis

Melum et al., 2024, Current Biology *34*, 632–640
February 5, 2024
https://doi.org/10.1016/j.cub.2023.12.042

CellPress

CellPress
OPEN ACCESS

Current Biology

Report

Hypothalamic tanycytes as mediators of maternally programmed seasonal plasticity

Vebjørn J. Melum,[1,4] **Cristina Sáenz de Miera,**[2] **Fredrik A.F. Markussen,**[1] **Fernando Cázarez-Márquez,**[1] **Catherine Jaeger,**[4] **Simen R. Sandve,**[3] **Valérie Simonneaux,**[4] **David G. Hazlerigg,**[1,5,7,*] **and Shona H. Wood**[1,5,6,7,8,*]
[1]Arctic seasonal timekeeping initiative (ASTI), UiT—The Arctic University of Norway, Department of Arctic and Marine Biology, Arctic Chronobiology and Physiology Research Group, NO-9037 Tromsø, Norway
[2]University of Michigan Medical School, Department of Molecular and Integrative Physiology, Ann Arbor, MI 48109, USA
[3]Faculty of Biosciences, Norwegian University of Life Sciences (NMBU), NO-1432 Ås, Norway
[4]University of Strasbourg, Institute of Cellular and Integrative Neurosciences, Strasbourg 67000, France
[5]X (formerly Twitter): @ArcticSeasonal
[6]X (formerly Twitter): @WoodLab_Arctic
[7]These authors contributed equally
[8]Lead contact
*Correspondence: david.hazlerigg@uit.no (D.G.H.), shona.wood@uit.no (S.H.W.)
https://doi.org/10.1016/j.cub.2023.12.042

SUMMARY

In mammals, maternal photoperiodic programming (MPP) provides a means whereby juvenile development can be matched to forthcoming seasonal environmental conditions.[1–4] This phenomenon is driven by *in utero* effects of maternal melatonin[5–7] on the production of thyrotropin (TSH) in the fetal *pars tuberalis* (PT) and consequent TSH receptor-mediated effects on tanycytes lining the 3rd ventricle of the mediobasal hypothalamus (MBH).[8–10] Here we use LASER capture microdissection and transcriptomic profiling to show that TSH-dependent MPP controls the attributes of the ependymal region of the MBH in juvenile animals. In Siberian hamster pups gestated and raised on a long photoperiod (LP) and thereby committed to a fast trajectory for growth and reproductive maturation, the ependymal region is enriched for tanycytes bearing sensory cilia and receptors implicated in metabolic sensing. Contrastingly, in pups gestated and raised on short photoperiod (SP) and therefore following an over-wintering developmental trajectory with delayed sexual maturation, the ependymal region has fewer sensory tanycytes. Post-weaning transfer of SP-gestated pups to an intermediate photoperiod (IP), which accelerates reproductive maturation, results in a pronounced shift toward a ciliated tanycytic profile and formation of tanycytic processes. We suggest that tanycytic plasticity constitutes a mechanism to tailor metabolic development for extended survival in variable overwintering environments.

RESULTS AND DISCUSSION

Maternal photoperiod profoundly affects offspring developmental trajectory and the tanycytic transcriptome

Wild Siberian hamsters (*Phodopus sungorus*) and other short-lived rodents use both the duration and direction of change of photoperiod to determine whether juveniles follow a fast, breeding or a slow, overwintering trajectory[1–4] (Figure 1A). To mimic this in the lab, we used a breeding protocol (Figure 1B) in which conception on long photoperiods (LPs, 16-h light/24 h) is followed by exposure to either LP or short photoperiod (SP, 8-h light/24 h) through pregnancy to weaning at postnatal day (pn) 21, followed by a continuation on these photoperiods or transfer to an intermediate photoperiod (IP, 14-h light/24 h) to the end of the study (pn50). This produced 4 distinctive trajectories of early-life photoperiodic history: steady-state long photoperiod (LP), declining photoperiod (LPIP), steady-state short photoperiod (SP), and increasing photoperiod (SPIP) (Figure 1B). In line with previously published work,[8] the response to these regimes revealed the interactive effects of photoperiod exposure pre- and post-weaning. Steady-state LP animals reached the largest size and had the largest testes, and steady-state SP animals the smallest, reflecting the pre- and post-weaning photoperiodic experience (Figures 1C and 1D). Transfer of LP-gestated pups to IP arrested growth and reproductive maturation, whereas transfer of SP-gestated pups to IP had the opposite effect, stimulating gonadal development and increased somatic growth (Figures 1C and 1D). Hence the developmental trajectory in the juvenile period depends on the interactive effects of photoperiod during gestation and post-weaning.

Previous work demonstrates that this photoperiodic programming is a melatonin-dependent phenomenon involving transplacental actions of melatonin *in utero*, which then modulate pup sensitivity to photoperiod in the post-weaning phase.[5–7] Melatonin acts via MT1 receptors in the pup *pars tuberalis* (PT) to control photoperiod-dependent production of the glycoprotein

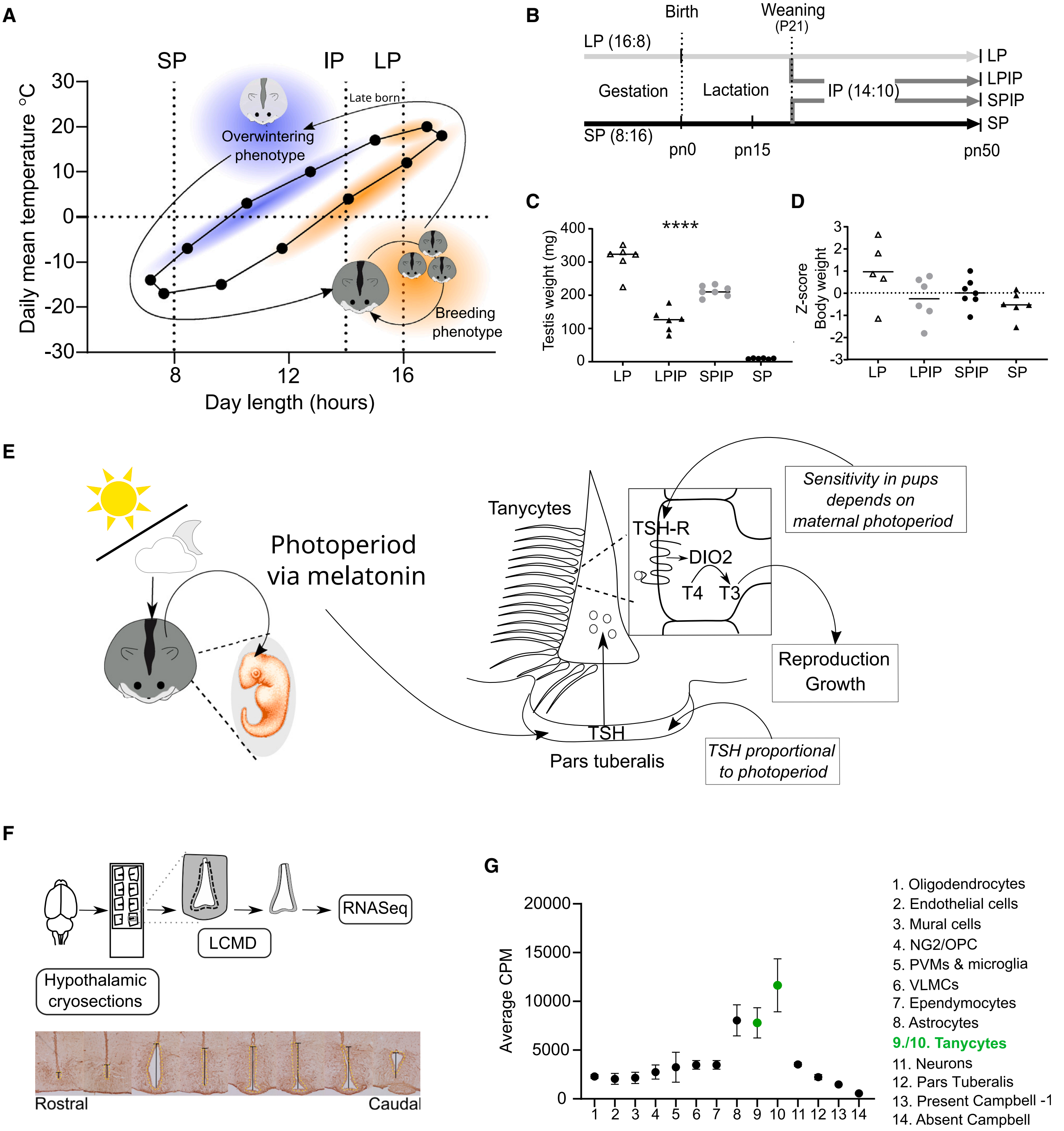

Figure 1. History-dependent effects of photoperiod on early-life developmental trajectory in Siberian hamsters (*Phodopus sungorus*)

(A) Elliptical relationship between the annual cycles of photoperiod and temperature in the natural habitat (55°N, Kazakhstan) and the influence on pup developmental trajectories. Pups born in spring to mid-summer are exposed to increasing/long photoperiods from conception and develop rapidly, allowing a further round of reproduction in the same year. Pups born in the late summer to autumn develop an overwintering phenotype (including white fur and expression of daily torpor) and delay breeding until the following spring.

(B) Experimental photoperiod manipulation paradigm to generate pups following divergent developmental trajectories mimicking the natural phenomenon. Adult females were gestated on a long (16-h light, 8-h dark [16:8]) or short photoperiod (8:16). At birth the mothers and pups were maintained on the gestation photoperiod. At weaning/postnatal day 21 (pn21), the pups were either maintained on the gestational photoperiods or transferred to an intermediate photoperiod (IP; 14:10). Animals were sampled at pn50.

(C) Testis weights in milligrams for each individual in each experimental group: long photoperiod (LP), long photoperiod transferred to intermediate photoperiod (LPIP), short photoperiod transferred to intermediate photoperiod (SPIP), and short photoperiod (SP). ****$p < 0.0001$ using a one-way ANOVA.

(D) Distribution of body weights of individual pups normalized to the pooled mean body mass (expressed as *Z* score).

(legend continued on next page)

hormone, thyrotropin (TSH), which in turn acts on TSH receptor (TSH-R)-expressing tanycytes lining the 3rd ventricle (3v) of the neighboring mediobasal hypothalamus (MBH) (Figure 1E).[8–10] Since we found previously that the level of TSH expression in the PT of hamster pups directly reflects current photoperiod, while tanycytic sensitivity to central injections of TSH at 50 days of age depends on photoperiodic history,[8] we hypothesized that the encoding of seasonal time depends on maternal photoperiodic effects on the development of tanycytes.

We performed RNA sequencing (RNA-seq) on LASER capture microdissected tissue from the tanycytic periventricular region, defined by expression of the intermediate filament protein vimentin (Figures 1F and S1). Using a single-cell RNA-seq[11] dataset, we confirmed that our approach yielded a tanycyte-enriched transcriptome (Figure 1G). Photoperiod treatment had a profound effect on the tanycytic transcriptome, with over 30% of all detectable transcripts showing significant changes in expression ($FDR < 0.01$). Nearly 60% of transcriptome-wide, between-sample variation in gene expression was accounted for by a single principal component, resolving samples according to photoperiod treatment (Figure 2A). These transcriptomic changes are far more pronounced than those reported in previous studies performed on whole hypothalamic blocks from Siberian hamsters or seasonally breeding sheep,[12–14] suggesting that photoperiodic effects on the tanycyte phenotype are the originators of seasonal neuroendocrine responses.

LP-gestated and -raised animals have more sensory ciliated tanycytes

We found 1,553 genes with increased expression under LP compared to SP ($FDR < 0.001$) (Figure 2B; Data S1B). Among these, strong enrichment for genes linked to the GO term "Cilium" (GO:0005929, FDR 2.86×10^{-12}) and to the GO process "Cilium assembly" (GO:0060271, FDR 9.21×10^{-4}) (Figure 2C; Table S1) suggests that the tanycytic presentation of cilia into the lumen of the 3rd ventricle is a photoperiod-dependent phenotype. Since ciliary function depends heavily on ciliary membrane lipids,[15] the heightened expression of genes including apolipoprotein E under LP, giving rise to strong enrichment for the GO term "High-Density Lipoprotein" (GO:0034364, FDR 9.57×10^{-3}), is also consistent with this interpretation.

To test whether photoperiod altered the abundance of cilia, we used immunological markers for cilia projections (acetylated α-tubulin) and basal bodies (γ-tubulin) to stain coronal and ventricular face hypothalamic sections from LP- and SP-reared hamsters (Figures 2D–2F and S2). In the putative α-tanycyte region, we found on average 4 times more basal bodies in LP-reared compared to SP-reared animals (Figures 2D and 2E; $p = 0.002$ by unpaired t test). The ventricular face sections confirm these findings showing an increased intensity in cilia projection staining and more distinct basal bodies in LP animals compared to SP animals (Figure 2F). The same trend was observed in the putative β-tanycyte region, albeit to a lesser extent (Figures S2C and S2D; 2-fold difference, $p < 0.05$ by unpaired t test). Collectively, these data demonstrate a profound effect of early life photoperiod on ciliary assembly in the tanycytic region.

Variable presence of sensory cilia on the apical surfaces of tanycytes likely leads to differences in sensory function through altered presentation of cell surface receptors and coupling to signal transduction machinery,[16–19] and this has been linked to the function of several G protein-coupled receptors (GPCRs).[18,20] This may account for the photoperiodic history-dependent differences in tanycyte TSH sensitivity between LP- and SP-gestated hamsters,[8] and may also be linked to the expression of a wide repertoire of GPCRs in the tanycytic transcriptome, many of which show photoperiod-dependent changes in RNA expression (Figure 2G). Of these, *gpr50*, the most abundantly expressed GPCR in the tanycyte transcriptome, shows the largest photoperiodic response, with expression levels an order of magnitude higher under LP. Along with previous metabolic studies in *gpr50* null mice,[21] this result implicates *gpr50* signaling in the photoperiodic programming of metabolic phenotype in juvenile hamsters. While cilia also provide a scaffold for sonic hedgehog (SHH) signaling (reviewed in Wheway et al., Anvarian et al., and Schou et al.[16,17,22]), and the expression of *shh* in the MBH of sheep varies with seasonal status,[13,14,23] we only saw modest effects on SHH pathway genes in the present study (Figures S3A and S3B). Overall, these profound effects on ciliation and expression of GPCRs suggest that early-life photoperiod modulates tanycytic sensitivity to metabolic feedback signals in the cerebrospinal fluid (CSF).

Plasticity of tanycytic phenotype in response to post-weaning photoperiodic change

Transferring animals to IP at weaning has opposite effects on the developmental trajectories of LP- and SP-reared animals: testis growth is arrested in the former and accelerated in the latter (Figure 1B).[8] As a result, by pn50, mean testes and body weights in LPIP animals were lower than those in SPIP animals. On the premise that this photoperiodic history-dependent modulation of post-weaning pup development stems from effects at the level of tanycytes, we explored the effects of post-weaning changes in photoperiod on the tanycyte transcriptome.

Transfer to IP has highly asymmetric effects on the transcriptional profile of the tanycytic region (Figure 3A; Data S1C–S1E), with a post-weaning increase in photoperiod (SPIP versus SP contrast) producing almost an order of magnitude more differentially expressed genes (DEGs) than is the case for a post-weaning decrease in photoperiod (LPIP versus LP contrast). Previously we showed that post-weaning suppression of gonadal growth and FSH secretion occurs in LPIP animals within 3 days following transfer to IP whereas activation of gonadal growth in SP-gestated pups emerges over the following month.[8]

(E) Melatonin-based photoperiodic relay mechanism operative in gestation interacts with direct perception of photoperiod by weaned pups. Maternal melatonin and pup melatonin engage sequentially with neuroendocrine control of pup development via the *pars tuberalis* and the tanycytes of the pups.

(F) Workflow to generate photoperiod-dependent tanycyte transcriptomes: Siberian hamster brains were sampled at pn50 and cryosectioned, and the vimentin-positive region surrounding the 3rd ventricle was LASER capture microdissected and processed for Illumina RNA-seq. See also Figure S1.

(G) Average counts per million (cpm) across all samples for all genes defined by Campbell et al.[11] as cell-type-specific cluster markers. Error bars indicate the SEM.

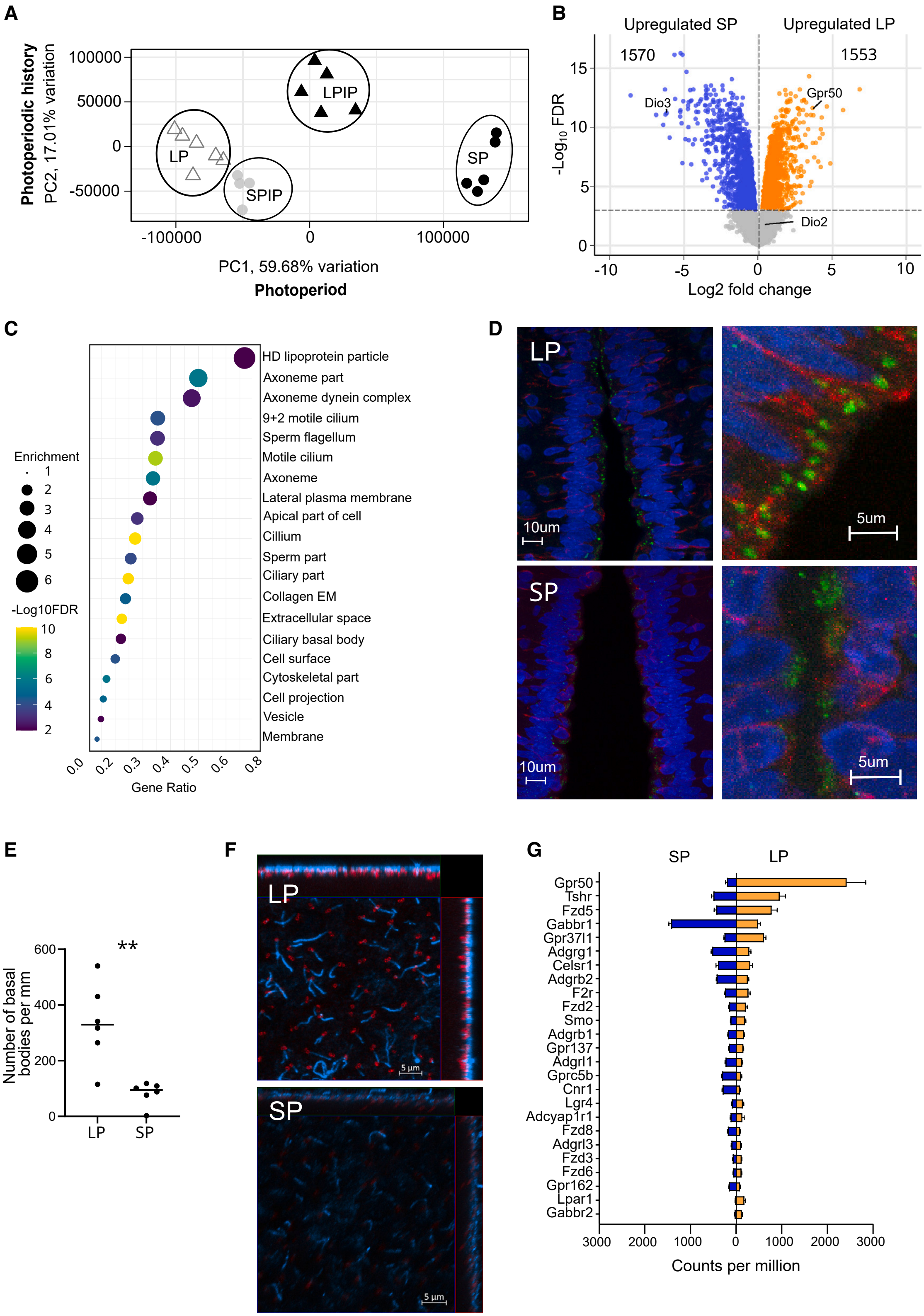

Figure 2. Photoperiodic effects on the tanycytic transcriptome and ciliary assembly

(A) Principal component analysis (PCA) plot showing the variation on the first two principal components for the entire transcriptome for all samples. Black circles, SP animals; gray circles, SPIP; black triangles, LPIP; white triangles, LP.

(legend continued on next page)

These findings suggest that a process of developmental remodeling of the ependymal region of the MBH precedes overt phenotypic changes in SPIP animals, whereas shutdown of reproductive development in LPIP animals reflects acute changes in the function of established feedback control circuits.

To characterize mechanisms involved in remodeling of the tanycytic region in SPIP animals, we looked for DEGs particularly associated with increasing photoperiod. Hence, we identified 109 DEGs for the SP versus SPIP contrast, which were not present in the SP versus LP contrast (FDR < 0.001 cut-off). This short list includes 4 upregulated genes linked to ciliogenesis (*ttc30a*, *kiz*, *rimbp3b*, and *ptpdc1*) and 4 key elements of FGF-signaling pathways implicated in migration of neural progenitors (*fgf18*, *cspg5*, *htra1*, and *chst11*)[25–28] (Figure 3B).

In the most common laboratory mouse strains (i.e., photoperiod-insensitive laboratory rodent models[29]), the cell-division phase of hypothalamic neurogenesis is essentially complete by the end of the neonatal period, and the juvenile period is a phase of establishment of neuronal connectivity.[30–32] Consistent with this model, while we see considerable numbers of MBH cells staining positively for the cell division markers PCNA and Ki67 in neonatal hamsters, this staining has disappeared almost completely by pn50 (Figures 3C and S3C). Furthermore, we see no effects of photoperiod treatment on the very limited numbers of positively stained cells beyond pn15 (Figure S3C). This suggests a model in which post-weaning photoperiodic remodeling in SPIP animals does not stem from effects on cell division per se, but rather on differentiation or migration of postmitotic cells.

Recently, Yoo and colleagues combined cell fate mapping and single-nucleus (sn)RNA-seq to define a set of 6 clusters characterizing the differentiation of tanycytes into tanycyte-derived neurons, each defined by approximately 1,000 to 2,000 cluster marker genes.[24] While we were able to identify approximately 90% of these markers in our RNA-seq dataset (9,141 genes), the relative levels of cluster marker gene expression differed profoundly between LP- and SP-reared animals (Figure 3D). Expression of cluster markers for differentiated tanycytes (i.e., ciliated cells, staining positively for the intermediate filament protein vimentin[32,33,34]) was markedly higher in LP-reared animals, while markers for tanycyte-derived neurons were increased in SP-reared animals.

Strikingly, cluster marker expression in SP-gestated animals was profoundly affected by post-weaning transfer to IP but was almost completely unaffected by transfer from LP to IP (Figure 3D). In support of this picture of remodeling and changing tanycyte phenotype, we observed clear photoperiodic effects on the extent and intensity of vimentin staining (Figures 3E and S3D).

The accepted model for relay of photoperiodic information in seasonal mammals sees TSH production by the PT driving a flip-flop switch between tanycytic states of high active thyroid hormone (T_3), high retinoic acid (RA) (LP, summer state) and low T_3, low RA (SP, winter state) (Figure 1E).[35–37] This is mediated through reciprocal effects on the expression of thyroid hormone deiodinases (*dio2* versus *dio3*) and retinol-metabolizing enzymes (*aldh1a1* versus *cyp26b1*), for which we see clear inverse regulation in hamster pups undergoing SPIP and LPIP transitions (Figure 3F). Hence the model predicts that transcriptomic responses to photoperiod in the tanycytic region stem from interactive effects of RA-/T_3-dependent nuclear hormone receptor signaling, mediated by ligand-dependent heterodimeric interactions between nuclear thyroid hormone receptors (TRα/β), retinoic acid receptors (RARα/β), and retinoid X receptors (RXR).[38] Consistent with this model, we found strong statistical enrichment for thyroid response elements (TREs) and retinoic acid response elements (RAREs) in genes induced or repressed by the SP to IP transition, and to a lesser extent following the LP to IP transition (Table S2). Among the SPIP-induced genes, the most enriched in terms of the combined total of TREs and RAREs is *arrb1* (β-arrestin), which is a key mediator of GPCR de-/re-sensitization[39–41] (Figure 3G). Our analysis also revealed many other enriched response elements in the sets of genes responsive to transfer to IP (Table S2), suggesting that T_3/RA signals initiate a complex cascade response to photoperiodic change.

A hypothalamic substrate for phenological plasticity

Pathologies that impair ciliary assembly are associated with increased fat deposition in mice,[20] and transgenic targeting of ciliary assembly in hypothalamic neurons leads to obesity through insensitivity to metabolic feedback signals.[42] We speculate that by suppressing tanycytic assembly of sensory cilia, SP limits relay of positive metabolic feedback signals in the CSF to the hypothalamus of juvenile hamsters and thereby establishes a "rheostatic"[43] shift to a metabolic phenotype suited to overwintering survival. Our data demonstrate that the process by which

---

(B) Volcano plot for the LP versus SP comparison. Orange dots are genes upregulated in LP and blue dots are genes upregulated in SP (FDR < 0.001). The x axis is the $\log_2$ fold change and the y axis is the $-\log_{10}$ transformed FDR value. Cut-off line is at FDR = 0.001. The number of upregulated genes in SP and LP is represented. Labels show the responses of well-known photoperiodically regulated genes: *dio3*, *dio2*, and *gpr50*. See also Data S1A.

(C) Dot plot of non-redundant GO terms for genes upregulated in LP. The size of the dot represents the enrichment calculated using GOrilla analysis. The color of the dot represents the $-\log_{10}$ transformed FDR value for the enrichment. The x axis is the gene ratio (number of genes present in the input list and GO term divided by total number of genes within the GO term). See also Table S1.

(D) Immunohistochemistry for basal bodies of cilia (γ-tubulin, green), vimentin (red), and nuclei (DAPI, blue) on coronal sections. Images are z stack maximum projections. Scale bars are 10 or 5 μm, as indicated on the image. LP, long photoperiod; SP, short photoperiod. The region shown is 400–600 μm from the bottom of the median eminence, corresponding to the alpha tanycyte region. See also Figure S2A.

(E) Quantification of the number of basal bodies per millimeter of ventricular surface for 6 individuals per group. Statistical differences were assessed by two-tailed unpaired t test, **p = 0.0022. See also Figures S2C and S2D.

(F) Immunohistochemistry of the face of the 3rd ventricle. Basal bodies of the cilia (γ-tubulin, red) and ciliary projections (α-tubulin, blue). Images shown are z stack maximal projections. The images show the area of the ventricle face compatible with the coronal images shown in (D). The outer edges of the image show a side-on view of the z stack. Scale bars represent 5 μm. See also Figure S2B.

(G) GPCR expression in the tanycytic transcriptomes of SP- (blue) and LP- (orange) reared hamsters, ranked in descending order of mean abundance across all individual samples. Error bars represent the SEM. See also Figures S3A and S3B.

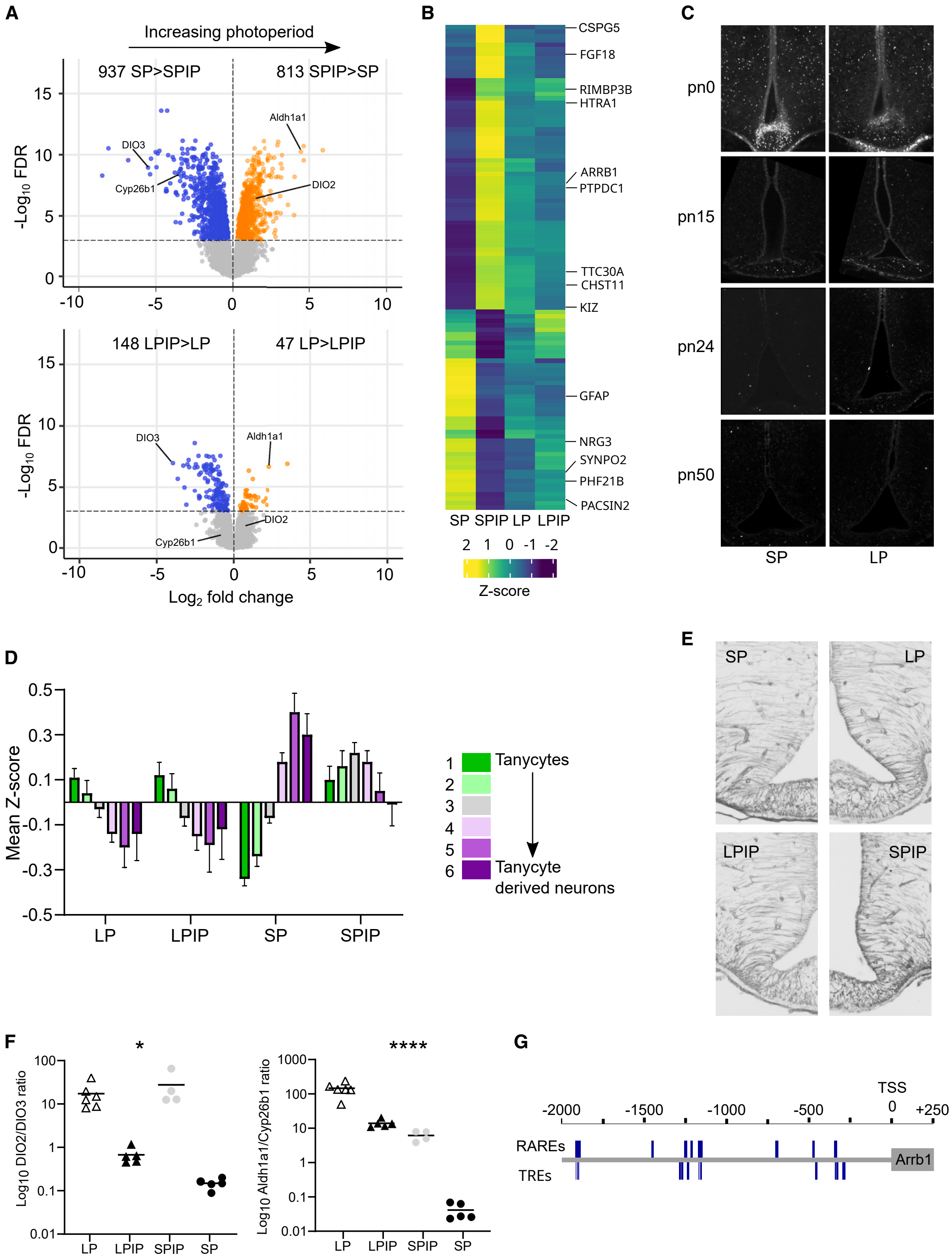

(legend on next page)

overwintering juveniles switch to a spring/summer phenotype following exposure to increasing photoperiod involves reorganization of the ependymal layer to establish a population of sensory tanycytes. Contrastingly, tissue reorganization appears less important for arrest of reproductive development by exposure to declining photoperiod. Along with our recent findings that gonadal development and tanycytic gene expression are more temperature sensitive in voles reared on an autumn photoperiodic regime than on a spring regime,[44,45] these data lead us to propose that the tanycytic region is the key hypothalamic substrate for phenological plasticity in mammals.

STAR★METHODS

Detailed methods are provided in the online version of this paper and include the following:

- KEY RESOURCES TABLE
- RESOURCE AVAILABILITY
    - ○ Lead contact
    - ○ Materials availability
    - ○ Data and code availability
- EXPERIMENTAL MODEL AND SUBJECT DETAILS
    - ○ Siberian hamsters
- METHOD DETAILS
    - ○ *Phodopus sungorus* genome sequencing
    - ○ LASER capture microdissection of tanycytes
    - ○ LCMD-RNA-seq, mapping and counts
    - ○ Gene expression analysis
    - ○ Transcription factor binding site analysis
    - ○ Immunohistochemistry
    - ○ Third ventricle face whole mounts for cilia
    - ○ PCNA & Ki67 staining
- QUANTIFICATION AND STATISTICAL ANALYSIS

SUPPLEMENTAL INFORMATION

Supplemental information can be found online at https://doi.org/10.1016/j.cub.2023.12.042.

ACKNOWLEDGMENTS

The work was supported by grants from the Tromsø Forskningsstiftelse (TFS) starter grant (TFS2016SW) and the TFS infrastructure grant (IS3_17_SW) awarded to S.H.W., Research Council of Norway Overseas research grant (Hypothalamic tanycytes as epigenetic calendars) awarded to S.H.W., Fonds Paul Mandel pour les recherches en neurosciences (Hypothalamic tanycytes as epigenetic calendars) awarded to S.H.W. and V.S., and University of Strasbourg Institute for Advanced Studies fellowship (project: Epigenetic light) awarded to D.G.H. The Arctic Seasonal Timekeeping Initiative (ASTI) grant and UiT strategic funds support D.G.H., S.H.W., F.A.F.M., and F.C.-M. The authors would like to acknowledge the National Infrastructure for Research Data (NIRD) project number nn9893k for use of the computing cluster SAGA to complete the bioinformatic analysis. In addition, we acknowledge the assistance of the Elixir-Norway project (https://elixir.no) (Elixir3, 322392) and, specifically, Lars Grønvold and Thu-Hien To for their assistance with the transcription factor binding site analysis. We thank Cristina Sandu for help in setting up and performing the initial microdissection tests and validation. Finally, we acknowledge the UiT core microscopy facility for the use of the confocal microscope.

AUTHOR CONTRIBUTIONS

Conceptualization, D.G.H., S.H.W., V.S., and C.S.d.M.; methodology, V.J.M., C.S.d.M., C.J., F.A.F.M., F.C.-M., S.R.S., and S.H.W.; software, S.R.S.; validation, C.J., C.S.d.M., F.A.F.M., and F.C.-M.; formal analysis, V.J.M., S.H.W., S.R.S., and D.G.H.; investigation, V.J.M., C.S.d.M., V.S., C.J., F.C.-M., F.A.F.M., and S.H.W.; resources, V.S. and S.H.W.; data curation, S.H.W., S.R.S., and V.J.M.; writing – original draft, S.H.W., D.G.H., and V.J.M.; writing – review & editing, all authors; visualization, S.H.W. and D.G.H.; supervision, S.H.W., D.G.H., and V.S.; project administration, V.S. and S.H.W.; funding acquisition, S.H.W., D.G.H., and V.S.

DECLARATION OF INTERESTS

The authors declare no competing interests.

Received: April 22, 2023
Revised: November 7, 2023
Accepted: December 13, 2023
Published: January 12, 2024

REFERENCES

1. Horton, T.H. (1984). Growth and maturation in Microtus montanus: effects of photoperiods before and after weaning. Can. J. Zool. *62*, 1741–1746.
2. Horton, T.H. (1984). Growth and reproductive development of male Microtus montanus is affected by the prenatal photoperiod. Biol. Reprod. *31*, 499–504.
3. Negus, N.C., Berger, P.J., and Brown, B.W. (1986). Microtine population dynamics in a predictable environment. Can. J. Zool. *64*, 785–792.
4. Negus, N.C., Berger, P.J., and Forslund, L.G. (1977). Reproductive strategy of Microtus montanus. J. Mammal. *58*, 347–353.

Figure 3. Increasing photoperiod post-weaning promotes tissue reorganization in the tanycytic region

(A) Volcano plots for post-weaning photoperiodic increase (SP to IP transition, upper panel) and decrease (LP to IP transition, lower panel); the dotted horizontal line indicates the FDR = 0.001 threshold. Data are presented as $\log_2$ fold change, upregulated in long photoperiod (LP) in orange, downregulated in short photoperiod (SP) in blue. See also Data S1B.

(B) Heatmap of differential gene expression for 109 genes passing the significance threshold for the SP to IP transition, but not for the LP versus SP contrast. The group mean *Z* score is color-coded as indicated. See also Data S1B and S1E.

(C) Dark field micrographs of PCNA staining in the mediobasal hypothalamus of hamsters between birth (pn0) and 50 days of age (pn50). See also Figure S3C.

(D) Relative abundances of genes in clusters representing different stages of hypothalamic neural/glial differentiation defined by snRNA-seq.[24] The mean *Z* score for expression of marker genes within each cluster is shown for each of the 4 photoperiod treatments. Error bars represent the SEM. The bars are color-coded as indicated.

(E) Vimentin staining in the MBH of hamsters raised to pn50 on the indicated photoperiod regimes. Note increased staining at ependymal surface and in processes projecting from tanycytes into the parenchyma in LP and SPIP animals. See also Figure S3D.

(F) Reciprocal effects of photoperiod treatment on tanycytic expression of enzymes determining local production of T_3 and RA in the MBH, presented as ratios between enzymes governing synthesis (*dio2* for T_3 and *aldh1a1* for RA) and degradation (*dio3* for T_3 and *cyp26* for RA). Results of one-way ANOVA are shown: $^*p < 0.01$, $^{****}p < 0.0001$.

(G) Detection of putative TREs and RAREs in the promoter region of *aarb1* (β-arrrestin). The figure shows the position of putative sites identified for JASPAR matrices in the 2 kb region upstream of the predicted transcription start site (TSS). See also Table S2.

5. Weaver, D.R., and Reppert, S.M. (1986). Maternal melatonin communicates day length to the fetus in djungarian hamsters. Endocrinology *119*, 2861–2863.
6. Horton, T.H., Stachecki, S.A., and Stetson, M.H. (1990). Maternal transfer of photoperiodic information in Siberian hamsters. IV. Peripubertal reproductive development in the absence of maternal photoperiodic signals during gestation. Biol. Reprod. *42*, 441–449.
7. Lee, T.M., Spears, N., Tuthill, C.R., and Zucker, I. (1989). Maternal melatonin treatment influences rates of neonatal development of meadow vole pups. Biol. Reprod. *40*, 495–502.
8. Saenz de Miera, C., Bothorel, B., Jaeger, C., Simonneaux, V., and Hazlerigg, D. (2017). Maternal photoperiod programs hypothalamic thyroid status via the fetal pituitary gland. Proc. Natl. Acad. Sci. USA *114*, 201702943.
9. Sáenz de Miera, C., Beymer, M., Routledge, K., Król, E., Selman, C., Hazlerigg, D.G., and Simonneaux, V. (2020). Photoperiodic regulation in a wild-derived mouse strain. J. Exp. Biol. *223*, jeb217687.
10. van Dalum, J., Melum, V.J., Wood, S.H., and Hazlerigg, D.G. (2019). Maternal photoperiodic programming: melatonin and seasonal synchronization before birth. Front. Endocrinol. *10*, 901.
11. Campbell, J.N., Macosko, E.Z., Fenselau, H., Pers, T.H., Lyubetskaya, A., Tenen, D., Goldman, M., Verstegen, A.M.J., Resch, J.M., McCarroll, S.A., et al. (2017). A molecular census of arcuate hypothalamus and median eminence cell types. Nat. Neurosci. *20*, 484–496.
12. Haugg, E., Borner, J., Diedrich, V., and Herwig, A. (2022). Comparative transcriptomics of the Djungarian hamster hypothalamus during short photoperiod acclimation and spontaneous torpor. FEBS Open Bio *12*, 443–459.
13. Lomet, D., Cognié, J., Chesneau, D., Dubois, E., Hazlerigg, D., and Dardente, H. (2018). The impact of thyroid hormone in seasonal breeding has a restricted transcriptional signature. Cell. Mol. Life Sci. *75*, 905–919.
14. Lomet, D., Druart, X., Hazlerigg, D., Beltramo, M., and Dardente, H. (2020). Circuit-level analysis identifies target genes of sex steroids in ewe seasonal breeding. Mol. Cell. Endocrinol. *512*, 110825.
15. Nechipurenko, I.V. (2020). The enigmatic role of lipids in cilia signaling. Front. Cell Dev. Biol. *8*, 777.
16. Wheway, G., Nazlamova, L., and Hancock, J.T. (2018). Signaling through the primary cilium. Front. Cell Dev. Biol. *6*, 8.
17. Anvarian, Z., Mykytyn, K., Mukhopadhyay, S., Pedersen, L.B., and Christensen, S.T. (2019). Cellular signalling by primary cilia in development, organ function and disease. Nat. Rev. Nephrol. *15*, 199–219.
18. Mykytyn, K., and Askwith, C. (2017). G-protein-coupled receptor signaling in cilia. Cold Spring Harb. Perspect. Biol. *9*, a028183.
19. Gerdes, J.M., Davis, E.E., and Katsanis, N. (2009). The vertebrate primary cilium in development, homeostasis, and disease. Cell *137*, 32–45.
20. Loktev, A.V., and Jackson, P.K. (2013). Neuropeptide Y family receptors traffic via the Bardet-Biedl syndrome pathway to signal in neuronal primary cilia. Cell Rep. *5*, 1316–1329.
21. Ivanova, E.A., Bechtold, D.A., Dupré, S.M., Brennand, J., Barrett, P., Luckman, S.M., and Loudon, A.S.I. (2008). Altered metabolism in the melatonin-related receptor (GPR50) knockout mouse. Am. J. Physiol. Endocrinol. Metab. *294*, E176–E182.
22. Schou, K.B., Pedersen, L.B., and Christensen, S.T. (2015). Ins and outs of GPCR signaling in primary cilia. EMBO Rep. *16*, 1099–1113.
23. Wood, S.H., Christian, H.C., Miedzinska, K., Saer, B.R.C., Johnson, M., Paton, B., Yu, L., McNeilly, J., Davis, J.R.E., McNeilly, A.S., et al. (2015). Binary switching of calendar cells in the pituitary defines the phase of the circannual cycle in mammals. Curr. Biol. *25*, 2651–2662.
24. Yoo, S., Kim, J., Lyu, P., Hoang, T.V., Ma, A., Trinh, V., Dai, W., Jiang, L., Leavey, P., Duncan, L., et al. (2021). Control of neurogenic competence in mammalian hypothalamic tanycytes. Sci. Adv. *7*, eabg3777.
25. Bernfield, M., Götte, M., Park, P.W., Reizes, O., Fitzgerald, M.L., Lincecum, J., and Zako, M. (1999). Functions of cell surface heparan sulfate proteoglycans. Annu. Rev. Biochem. *68*, 729–777.
26. Sirko, S., von Holst, A., Weber, A., Wizenmann, A., Theocharidis, U., Götz, M., and Faissner, A. (2010). Chondroitin sulfates are required for fibroblast growth factor-2-dependent proliferation and maintenance in neural stem cells and for epidermal growth factor-dependent migration of their progeny. Stem Cell. *28*, 775–787.
27. Cortes, M., Baria, A.T., and Schwartz, N.B. (2009). Sulfation of chondroitin sulfate proteoglycans is necessary for proper Indian hedgehog signaling in the developing growth plate. Development *136*, 1697–1706.
28. Kim, G.-Y., Kim, H.-Y., Kim, H.-T., Moon, J.-M., Kim, C.-H., Kang, S., and Rhim, H. (2012). HtrA1 is a novel antagonist controlling fibroblast growth factor (FGF) signaling via cleavage of FGF8. Mol. Cell Biol. *32*, 4482–4492.
29. Kasahara, T., Abe, K., Mekada, K., Yoshiki, A., and Kato, T. (2010). Genetic variation of melatonin productivity in laboratory mice under domestication. Proc. Natl. Acad. Sci. USA *107*, 6412–6417.
30. Bouret, S.G., and Simerly, R.B. (2006). Developmental programming of hypothalamic feeding circuits. Clin. Genet. *70*, 295–301.
31. Bouret, S.G. (2022). Developmental programming of hypothalamic melanocortin circuits. Exp. Mol. Med. *54*, 403–413.
32. Altman, J., and Bayer, S.A. (1978). Development of the diencephalon in the rat. III. Ontogeny of the specialized ventricular linings of the hypothalamic third ventricle. J. Comp. Neurol. *182*, 995–1015.
33. Mirzadeh, Z., Kusne, Y., Duran-Moreno, M., Cabrales, E., Gil-Perotin, S., Ortiz, C., Chen, B., Garcia-Verdugo, J.M., Sanai, N., and Alvarez-Buylla, A. (2017). Bi- and uniciliated ependymal cells define continuous floor-plate-derived tanycytic territories. Nat. Commun. *8*, 13759.
34. Rodríguez, E.M., Blázquez, J.L., Pastor, F.E., Peláez, B., Peña, P., Peruzzo, B., and Amat, P. (2005). Hypothalamic tanycytes: a key component of brain–endocrine interaction. Int. Rev. Cytol. *247*, 89–164.
35. Hazlerigg, D., and Simonneaux, V. (2015). Seasonal regulation of reproduction in mammals. In Knobil and Neill's Physiology of Reproduction (Elsevier), pp. 1575–1604.
36. West, A.C., and Wood, S.H. (2018). Seasonal physiology: making the future a thing of the past. Curr. Opin. Physiol. *5*, 1–8.
37. Shearer, K.D., Goodman, T.H., Ross, A.W., Reilly, L., Morgan, P.J., and McCaffery, P.J. (2010). Photoperiodic regulation of retinoic acid signaling in the hypothalamus. J. Neurochem. *112*, 246–257.
38. Evans, R.M., and Mangelsdorf, D.J. (2014). Nuclear receptors, RXR, and the Big Bang. Cell *157*, 255–266.
39. Gurevich, V.V., and Gurevich, E.V. (2019). GPCR signaling regulation: the role of GRKs and Arrestins. Front. Pharmacol. *10*, 125.
40. Jean-Charles, P.-Y., Kaur, S., and Shenoy, S.K. (2017). G protein–coupled receptor signaling through β-arrestin–dependent mechanisms. J. Cardiovasc. Pharmacol. *70*, 142–158.
41. Thomsen, A.R.B., Plouffe, B., Cahill, T.J., Shukla, A.K., Tarrasch, J.T., Dosey, A.M., Kahsai, A.W., Strachan, R.T., Pani, B., Mahoney, J.P., et al. (2016). GPCR-G protein-β-arrestin super-complex mediates sustained G protein signaling. Cell *166*, 907–919.
42. Volta, F., and Gerdes, J.M. (2017). The role of primary cilia in obesity and diabetes. Ann. N. Y. Acad. Sci. *1391*, 71–84.
43. Mrosovsky, N. (1990). Rheostasis: The Physiology of Change, 1st ed. (Oxford University Press).
44. van Rosmalen, L., van Dalum, J., Appenroth, D., Roodenrijs, R.T.M., de Wit, L., Hazlerigg, D.G., Hut, R.A., van Rosmalen, L., van Dalum, J., Appenroth, D., et al. (2021). Mechanisms of temperature modulation in mammalian seasonal timing. FASEB J *35*, e21605.
45. van Dalum, M.J., van Rosmalen, L., Appenroth, D., Cazarez Marquez, F., Roodenrijs, R.T.M., de Wit, L., Hut, R.A., and Hazlerigg, D.G. (2023). Ambient temperature effects on the spring and autumn somatic growth trajectory show plasticity in the photoneuroendocrine response pathway in the tundra vole. J. Biol. Rhythms *38*, 586–600.
46. Castro-Mondragon, J.A., Riudavets-Puig, R., Rauluseviciute, I., Lemma, R.B., Turchi, L., Blanc-Mathieu, R., Lucas, J., Boddie, P., Khan, A., Manosalva Pérez, N., et al. (2022). JASPAR 2022: the 9th release of the

open-access database of transcription factor binding profiles. Nucleic Acids Res. *50*, D165–D173.

47. Chen, S., Zhou, Y., Chen, Y., and Gu, J. (2018). fastp: an ultra-fast all-in-one FASTQ preprocessor. Bioinformatics *34*, i884–i890.
48. Kolmogorov, M., Yuan, J., Lin, Y., and Pevzner, P.A. (2019). Assembly of long, error-prone reads using repeat graphs. Nat. Biotechnol. *37*, 540–546.
49. Li, H. (2018). Minimap2: pairwise alignment for nucleotide sequences. Bioinformatics *34*, 3094–3100.
50. Shafin, K., Pesout, T., Chang, P.-C., Nattestad, M., Kolesnikov, A., Goel, S., Baid, G., Kolmogorov, M., Eizenga, J.M., Miga, K.H., et al. (2021). Haplotype-aware variant calling with PEPPER-Margin-DeepVariant enables high accuracy in nanopore long-reads. Nat. Methods *18*, 1322–1332.
51. Li, H., Handsaker, B., Wysoker, A., Fennell, T., Ruan, J., Homer, N., Marth, G., Abecasis, G., and Durbin, R.; 1000 Genome Project Data Processing Subgroup (2009). The Sequence Alignment/Map format and SAMtools. Bioinformatics *25*, 2078–2079.
52. Earl, D., Bradnam, K., St. John, J., Darling, A., Lin, D., Fass, J., Yu, H.O.K., Buffalo, V., Zerbino, D.R., Diekhans, M., et al. (2011). Assemblathon 1: a competitive assessment of de novo short read assembly methods. Genome Res. *21*, 2224–2241.
53. Manni, M., Berkeley, M.R., Seppey, M., and Zdobnov, E.M. (2021). BUSCO: assessing genomic data quality and beyond. Curr. Protoc. *1*, e323.
54. Shumate, A., and Salzberg, S.L. (2021). Liftoff: accurate mapping of gene annotations. Bioinformatics *37*, 1639–1643.
55. Langmead, B., and Salzberg, S.L. (2012). Fast gapped-read alignment with Bowtie 2. Nat. Methods *9*, 357–359.
56. Robinson, M.D., McCarthy, D.J., and Smyth, G.K. (2010). edgeR: a Bioconductor package for differential expression analysis of digital gene expression data. Bioinformatics *26*, 139–140.
57. Harding, S.D., Armstrong, J.F., Faccenda, E., Southan, C., Alexander, S.P.H., Davenport, A.P., Pawson, A.J., Spedding, M., and Davies, J.A.; NC-IUPHAR (2022). The IUPHAR/BPS guide to PHARMACOLOGY in 2022: curating pharmacology for COVID-19, malaria and antibacterials. Nucleic Acids Res. *50*, D1282–D1294.
58. Walker, B.J., Abeel, T., Shea, T., Priest, M., Abouelliel, A., Sakthikumar, S., Cuomo, C.A., Zeng, Q., Wortman, J., Young, S.K., and Earl, A.M. (2014). Pilon: an integrated tool for comprehensive microbial variant detection and genome assembly improvement. PLoS One *9*, e112963.
59. Butler, A.E., Matveyenko, A.V., Kirakossian, D., Park, J., Gurlo, T., and Butler, P.C. (2016). Recovery of high-quality RNA from laser capture microdissected human and rodent pancreas. J. Histotechnol. *39*, 59–65.
60. Wood, S.H., Craig, T., Li, Y., Merry, B., and de Magalhães, J.P. (2013). Whole transcriptome sequencing of the aging rat brain reveals dynamic RNA changes in the dark matter of the genome. Age *35*, 763–776.
61. Eden, E., Navon, R., Steinfeld, I., Lipson, D., and Yakhini, Z. (2009). GOrilla: a tool for discovery and visualization of enriched GO terms in ranked gene lists. BMC Bioinf. *10*, 48.
62. Wickham, H. (2016). ggplot2: Elegant Graphics for Data Analysis (Use R! Ser.).
63. Grant, C.E., Bailey, T.L., and Noble, W.S. (2011). FIMO: scanning for occurrences of a given motif. Bioinformatics *27*, 1017–1018.
64. Robinson, J.T., Thorvaldsdóttir, H., Winckler, W., Guttman, M., Lander, E.S., Getz, G., and Mesirov, J.P. (2011). Integrative genomics viewer. Nat. Biotechnol. *29*, 24–26.
65. Mclean, I.W., and Nakane, P.K. (1974). Periodate-lysine-paraformaldehyde fixative. A new fixation for immunoelectron microscopy. J. Histochem. Cytochem. *22*, 1077–1083.
66. Klosen, P., Maessen, X., and van den Bosch de Aguilar, P. (1993). PEG embedding for immunocytochemistry: application to the analysis of immunoreactivity loss during histological processing. J. Histochem. Cytochem. *41*, 455–463.
67. Morin, L.P., and Wood, R.I. (2001). A Stereotaxic Atlas of the Golden Hamster Brain (Elsevier Science).

STAR★METHODS

KEY RESOURCES TABLE

REAGENT or RESOURCE	SOURCE	IDENTIFIER
Antibodies		
Mouse anti-Vimentin	ThermoFisher	Cat# MA5-11883; RRID:AB_10985392
Rabbit anti γ-tubulin	Sigma-Aldrich	Cat# T5192; RRID:AB_261690
Goat anti-mouse Alexa Fluor 647	Abcam	Cat# ab150115; RRID:AB_2687948
Donkey anti-rabbit Alexa Fluor 488	Abcam	Cat# ab150073; RRID:AB_2636877
Mouse anti α-tubulin	Sigma-Aldrich	Cat# T6793; RRID:AB_477585
Goat Anti-Mouse Brilliant Violet 42	Jackson Immuno research	Cat# 115-675-166; RRID:AB_2651087
Rabbit anti-Ki67	Abcam	Cat# ab15580; RRID:AB_443209
Monoclonal anti-PCNA made in mouse	Abcam	Cat# ab29; RRID:AB_303394
Chemicals, peptides, and recombinant proteins		
Rnase inhibitor ProtectRNA 500x	Sigma-Aldrich	R7397
cold water fish skin gelatine	Sigma-Aldrich	G7041
bovine serum albumin	Sigma-Aldrich	A2153
tween 20	Sigma-Aldrich	P9416
TrueBlack lipofuscin autofluorescence quencher	Biotium	23007
Hoechst 33342 solution	ThermoFisher	62249
Dabco 33-LV reagent	Sigma-Aldrich	290734
Triton X-100	Sigma-Aldrich	T8787
SYTOX green	Thermo Fisher	S7020
Crystal Mount Aqueous Mounting Medium	Sigma-Aldrich	C0612
Normal horse serum	NHS; Vector Labs., Burlingame, CA, USA	S-2000-20
niquel-3,3-diaminobenzidine (Ni-DAB)	Sigma-Aldrich	D7304
Critical commercial assays		
Nanobind Tissue Big DNA Kit	Circulomics	102-302-100
SQK-LSK109 kit	Nanopore	SQK-LSK109
Qiagen all prep DNA/RNA micro kit	Qiagen	80284
Short Read Elimination Kit	Circulomics	EXP-SFE001
Vectastain Universal Elite ABC kit	Vector Labs.	PK-6200
Deposited data		
nanopore long read genome sequencing, illumina genome sequencing	This paper & Sequence read archive (SRA)	SRA: PRJNA839344
RNA-seq data	This paper & GEO	SRA: PRJNA842667; GEO: GSE204883
Genome assembly project	This paper & DDBJ/ENA/GenBank	GenBank: JANBXA000000000
Genome assembly statistics	This paper	DataverseNO: https://doi.org/10.18710/1IHNDD
Number of transcription factor binding sites in *Phodopus sungorus* genome	This paper	DAtaverseNO: https://doi.org/10.18710/1IHNDD
Comparative analysis between pseudotime clusters from mouse single RNAseq pseudotime analysis and our RNAseq dataset	This paper	DataverseNO: https://doi.org/10.18710/1IHNDD
Body and testis weight	This paper	DataverseNO: https://doi.org/10.18710/1IHNDD
Pseudotime clusters from snRNAseq in mice	Yoo et al.[24]	https://doi.org/10.1126/sciadv.abg3777
SnRNAseq data from the hypothalamus of mice	Campbell et al.[11]	https://doi.org/10.1038/nn.4495
Mouse GRCm39 ensembl release 104	Ensembl	Ensembl: https://www.ensembl.org/Mus_musculus/Info/Annotation

(*Continued on next page*)

Continued

REAGENT or RESOURCE	SOURCE	IDENTIFIER
JASPAR (JASPAR2022_CORE_non-redundant)	Castro-Mondragon et al.[46]	JASPAR: https://jaspar.elixir.no/
Curated list of GPCRs	IUPHAR	IUPHAR: https://www.guidetopharmacology.org/GRAC/ReceptorFamiliesForward?type=GPCR
Experimental models: Organisms/strains		
Siberian hamsters (*Phodopus sungorus*)	Chronobiotron UMS 3415	N/A
Software and algorithms		
R scripts for transcription factor binding site analysis	This paper	Github: https://doi.org/10.5281/zenodo.10285435
R scripts for differential expression analysis	This paper	Github: https://doi.org/10.5281/zenodo.10285435
Porechop ONT and fastp (genome assembly)	Chen et al.[47]	https://doi.org/10.1093/bioinformatics/bty560
Flye v2.8	Kolmogorov et al.[48]	https://doi.org/10.1038/s41587-019-0072-8
Minimap2	Li et al.[49]	https://doi.org/10.1093/bioinformatics/bty191
PEPPER	Shafin et al.[50]	https://doi.org/10.1038/s41592-021-01299-w
samtools	Li et al.[51]	https://doi.org/10.1093/bioinformatics/btp352
Assembly statistics script (assemblathon-stats.pl)	Earl et al.[52]	https://doi.org/10.1101/gr.126599.111
Busco v5.1	Berkeley et al.[53]	https://doi.org/10.1002/cpz1.323
Liftoff tool	Shumate et al.[54]	https://doi.org/10.1093/bioinformatics/btaa1016
Bowtie2	Langmead et al.[55]	https://doi.org/10.1038/nmeth.1923
R	R project	https://www.r-project.org/
EdgeR	Robinson et al.[56]	https://doi.org/10.1093/bioinformatics/btp616
GoRilla	Eden et al.[57]	https://doi.org/10.1186/1471-2105-10-48
FIMO tool (MEME suite) v. 5.4.1	Grant et al.[46]	https://doi.org/10.1093/bioinformatics/btr064
Zeiss zen	Zeiss	https://www.zeiss.com/microscopy/en/products/software/zeiss-zen.html#zenversions
Qupath	Qupath	https://qupath.github.io/
ImageJ	Wayne Rasband	https://ImageJ.nih.gov/ij/
Pilon v1.23	Walker et al.[58]	https://doi.org/10.1371/journal.pone.0112963
Graphpad prism	Graphpad software	https://www.graphpad.com/

RESOURCE AVAILABILITY

Lead contact

Further information and requests for resources and reagents should be directed to and will be fulfilled by the lead contact, Shona Wood (shona.wood@uit.no).

Materials availability

This study did not generate new unique reagents.

Data and code availability

- RNA-seq data from LASER captured tanycytes are available at SRA: PRJNA842667 and GEO: GSE204883 and are publicly available as of the date of publication. key resources table The nanopore long read genome sequencing and illumina genome sequencing used to generate the *Phodopus sungorus* genome have been deposited in the SRA: PRJNA839344 and are publicly available as of the date of publication. key resources table The genome assembly for *Phodopus sungorus* has been deposited in GenBank: JANBXA000000000 and are publicly available as of the date of publication. key resources table Genome assembly statistics for the *Phodopus sungorus* genome, the number of transcription factor binding site motifs identified in the *Phodopus sungorus* genome and the genes present in our dataset and the corresponding tanycyte cluster from the pseudotime analysis of Yoo et al.[24] have all been deposited as tables in DataverseNO: https://doi.org/10.18710/1IHNDD key resources table. All other analyzed data and confocal images reported in this paper will be shared by the lead contact upon request.
- R scripts and related files for differential gene expression and transcription factor binding site analysis are available on key resources table Github: https://doi.org/10.5281/zenodo.10285435
- Any additional information required to reanalyze the data reported in this paper is available from the lead contact upon request.

EXPERIMENTAL MODEL AND SUBJECT DETAILS

Siberian hamsters

Experiments were conducted in accordance with French National Law implementing the European Communities Council Directive 2010/63/EU and the French Directive 2013-118. All procedures were validated by the Animal Welfare Committee of the Animal Resource and Experimentation platform (Chronobiotron UMS 3415) of the Strasbourg Institute of Neuroscience.

Siberian hamsters (*Phodopus sungorus*) were mated on long photoperiod (LP — 16 h light:8 h dark (16:8)), before transfer of half of the pregnant females to SP (8:16). Dams and pups remained on the same photoperiod until weaning. From weaning, half of the animals in each litter remained on the same photoperiod and half were transferred to IP (14:10) (Figure 1A). All sample groups contained offspring from at least three different litters. Males were killed at postnatal day (pn) 0, 15, 24, and 50 in the mid-light phase. All animals were weighed before harvesting of tissues. Testis weight and body weight were recorded.

METHOD DETAILS

Phodopus sungorus genome sequencing

Livers collected for genome sequencing were snap frozen on chilled isopentane over liquid nitrogen and stored at -80°C. High molecular weight DNA was isolated from 27mg frozen liver using Nanobind Tissue Big DNA Kit from Circulomics. Extracted DNA was sheared using a 27G blunt end needle. The resulting DNA was sequenced using both long read nanopore sequencing and short read illumina sequencing for assembly polishing. For the long-read sequencing, size selection was performed by using the Short Read Elimination Kit from Circulomics. A sequencing library was made using the SQK-LSK109 kit, following the Genomic DNA by Ligation Nanopore Protocol. Library was sequenced on one Promethion flow cell (FLO-PRO002). Illumina sequencing of paired-end 150bp reads was performed by Novogene Fastq files used for genome assembly are available on SRA:PRJNA839344.

Figure S1A shows the bioinformatic pipeline for genome assembly. In brief, the long-read sequences were quality filtered and trimmed using porechop ONT and fastp.[47] The following parameters were used in fastp: -disable_trim_poly_g , -disable_adapter_trimming , -q 7, -l 4000, -f 50. This produced a total of 72,6 Gb porechop filtered data with an average read N50 of 50.5kb.

The *Phodopus sungorus* genome was assembled using flye v2.8[48] with three different overlap sizes (7k, 15k, 20k). We chose to continue with the 15k overlap assembly.

For error correction of the long reads sequences we first mapped raw long reads to the 15k overlap assembly using minimap2.[49] We then used PEPPER[50] to correct base errors in assembly using nanopore reads themselves, using the base calling model parameters: –model_path pepper_r941_guppy305_human.pkl. Finally, we performed a second round of assembly error correction using pilon v 1.23.[58] Here, the Illumina short reads were mapped to genome assembly using 'bwa mem' with default parameters. The resulting bam file was sorted using 'samtools sort'[51] command and then pilon v 1.23 was used with default parameters to correct remaining errors. This resulted in our final assembly; Psun-UiT-1 (Figure S1A) available in Genbank:JANBXA010000000. A script for summarizing the statistics for the assembly was used[52] (see key resources table), the results are found on DataverseNO: https://doi.org/10.18710/1IHNDD .

To check the quality of our assembly we used busco v5.1[53] with the vertebrata_odb10 conserved gene set to estimate gene space contiguity. Our assembly had a gene contiguity of 98.1%.

We annotated Psun-UiT-1 using the liftoff tool[54] and the mouse genome (Mouse GRCm39, Ensembl release 104) (Figure S1A). 21882 genes were annotated in our new genome.

LASER capture microdissection of tanycytes

The brains (6 per group) were snap frozen on chilled isopentane over liquid nitrogen and sectioned on the cryostat (-20°C; Leica CM3000) at 25μm. The brains were cut in series to allow the whole medio-basal hypothalamic region to be covered on one slide (Figure 1F). For LASER capture microdissection (LCMD) each animal had 5 – 6 PEN membrane frame slides (Arcturus, Thermo Fisher) slides of 12 sections and every 7th section was stained for vimentin (see immunohistochemistry subsection) to measure the ventral-dorsal length of vimentin expression, as a marker for tanycyte location. This measurement was used when microdissecting each series, to enrich for tanycytes. Slides were individually placed in pre-cooled 50 mL centrifuge tubes (Corning) on dry ice and stored at -80°C.

Immediately before LCMD the membrane frame slides were stained using cresyl violet and dehydrated based on Butler et al.[59] Unless stated all solutions contained Rnase inhibitor (ProtectRNA 500x, Sigma). In brief, frozen slides were rapidly defrosted at room temperature and placed in 0.2% cresyl violet in 70% ethanol for 1 min 30 s, then 30 s each of: 75% ethanol (twice), 95% ethanol and 100% ethanol. The final step was 2 min in 100% ethanol without Rnase inhibitor. From here the slides were air-dried for 5 min at room temperature and directly transferred to the laser microdissector (Veritas Microdissection Instrument, Model 704, Arcturus Bioscience) and microdissection was completed within 30 min to minimize RNA degradation. LCMD was carried out at x10. IR laser power of 70-100 mW and 2500 μsec of pulse (1 hit) were used to capture the tanycytes on the transfer film of the microdissection caps (Capsure Macro LCM caps, Arcturus) followed by UV laser power of 18 mW and 2 μm of spot size for cutting around the captured tissue.

We microdissected the tanycytic region of the 3rd ventricle within two to three cell bodies of the ventricle wall (Figure S1B) and limited to the dorsal length indicated by the vimentin staining. The microdissected tissues were collected in Rnase-free DNA lowbind tubes, snap frozen on dry ice and stored at -80°C. RNA was extracted from the microdissected tissue using the Qiagen all prep DNA/RNA micro kit according to the manufacturer's instructions. The RNA integrity numbers were determined by TapeStation high sensitivity RNA analysis and all were between 8.5 and 9.

LCMD-RNA-seq, mapping and counts

RNA-seq library construction was performed by BGI using their standard RNA-seq protocol and paired-end sequenced on an Illumina high seq 4000. Quality control checks and barcode removal were performed according to BGI protocol. Approximately 40 to 50 million reads were generated per sample. Mapping was performed on the Sigma2 national infrastructure for research data (NIRD) supercomputer SAGA. FASTQ files were mapped using bowtie2[55] and these parameters: bowtie2 -q —phred33 —fr -t -p 8 -x. Psun-UiT-1 genome assembly and Psun annotation we generated were used for the mapping (Figure S1C). This approach mapped un-spliced reads (as previously[23,60]) and gave a mapping rate which averaged 83%. Feature counts was used to count the mapped reads to genes, using these parameters: featureCounts -p -t exon -g gene_id (Figure S1C), on average 72% of alignments were assigned to an annotated feature.

FASTQ files and count files were deposited in key resources table GEO: GSE204883

Gene expression analysis

Differential expression analyses were performed using using Rstudio, and the package EdgeR.[56] We determined the median counts per million (CPM) across the whole experiment for each gene and applied a cut off of 10 raw counts (0.5 CPM in our study), removing genes with a median of less than one CPM from the analysis. 13346 genes remained representing our LCMD transcriptome, this dataset was used in all subsequent analysis.

In brief, a GLM analysis according to the EdgeR manual was conducted to determine which genes were differentially expressed between the groups (Data S1). Volcano plots of these data were generated using the enhanced volcano package. Throughout the analysis we used a FDR cut off of 0.001 and no log 2-fold change cut off.

A single nuclei RNA-seq dataset generated by Campbell et al.[11] determined cell type specific markers for genes in the hypothalamus. This list was used to categorize the genes expressed in our dataset into cell types. We averaged the counts per million across the experiment for the genes in those specific cell type clusters and plotted the data to show cell type enrichment in our dataset (Figure 1G).

The list of G-protein coupled receptors used in our analysis was from IUPHAR which has a curated list of all GPCR (7TMs) excluding olfactory receptors (n = 411).[57]

GO term enrichment analysis was performed using GORilla,[61] the expressed transcriptome was used as a background for the analysis. The enriched terms were filtered manually for redundancy and data were visualized using R and ggplot2[62] to create dot plots (Table S1; Figure 2C).

A single nuclei RNA-seq dataset generated by Yoo et al.[24] determined specific markers for the transition between alpha tanycytes and tanycyte derived neurons using pseudo time analysis. This identified 6 distinct cell type clusters. Using the genes listed within each cluster an individual Z score was calculated across the genes by taking the counts per million for each gene and each individual in our dataset. Then individual Z score within each cluster was used to create the mean Z score and standard deviation for each experimental group. The data were plotted using Graphpad prism 8 (Figure 3D).

Transcription factor binding site analysis

We downloaded TFBS motifs from the JASPAR database (JASPAR2022_CORE_non-redundant)[46] and scanned the entire genome for individual matches of all motifs using the FIMO tool from the MEME Suite (ver 5.4.1).[63] The FIMO tool was run with default settings, except for the parameter "—max-stored-scores", which was set to 1000000. Only motifs in the CORE_vertebrates database were used for downstream analyses.

For each gene promoter in the Psun genome (-2000/+200 bp from TSS) significant TFBS motif matches from FIMO were counted. The numbers of identified motifs in each gene found in our Psun assembly are available on DataverseNO: https://doi.org/10.18710/1IHNDD .

For each TFBS motif, a 2x2 contingency table was constructed summarizing the number of promoters with ≥1 and no matches in the SPIP unique DEGs or LPIP DEGs and in all other genes. These contingency tables were then used to tests for enrichment of TFBS motifs in promoters in genes either the SPIP unique DEGs or LPIP DEGs using the fisher.test function in R. Correction for multiple testing was carried out using the p.adjust function in R with the false discovery rate method. The odds ratios were calculated for each motif; (number of genes with motif "A" in the gene set of interest divided by number of genes with non "A" motif in the gene set of interest) divided by (number of genes with motif "A" in background divided by number of genes with non "A" motif in the background) (Table S2).

IGV browser[64] was used to view the position of the significant RARE and TRE motif matrixes in the promoter region of *arrb1*, a simplified representation is in Figure 3G.

Immunohistochemistry

Vimentin staining for LCMD

The slides were oven dried at 45°C for 5 min, fixed for 10 min with ice-cold paraformaldehyde 4% in phosphate buffer (PB), and then rinsed 3 times 5 min with Tris buffered saline (TBS). Blocking was performed with non-fat milk powder for 1 h and primary antibody incubation occurred overnight at 4°C with mouse anti-vimentin antibody (1:1000, ThermoFisher MA5-11883) in TBS-tween 20 (TBS-T20) containing 1% donkey serum and 0.1% NaN_3. The slides were then rinsed 3 times 10 min in TBS-T20 and incubated for 1-h with biotinylated donkey anti-mouse secondary antibody (1:1000) in TBS-T20 containing 1% donkey serum. After 3 times 10-min rinses in TBS-T20 and an additional 10-min rinse in TBS, the slides were stained for 5-10 min with DAB 1:100 in TBS. The slides were finally rinsed twice 5 min with tap water and covered with Crystal Mount Aqueous Mounting Medium (Sigma-Aldrich C0612). After overnight air drying, the slides were washed twice for 5 min in toluene, mounted with Eukitt Mounting Medium and imaged with a x5 objective.

Coronal sections for cilia

For immunohistochemistry, transcardiac perfusion was performed with periodate-lysine-paraformaldehyde.[65] The brain was dissected out and embedded in polyethylene glycol (PEG).[66] 10 μm coronal sections were obtained using a rotary microtome (Leitz 1512). PEG sections were rehydrated in a water bath and mounted on glass slides (Superfrost ultra plus gold, fisher scientific) dried at 50°C for 15 min and stored at -80°C until staining. Sections were rehydrated in distilled water and then 95°C trisodium citrate pH 6.0 for 60 min for antigen retrieval. Slides were cooled at room temperature for 45-60 min in antigen retrieval solution. Sections were rinsed in tris buffered saline (TBS pH 7.4). Non-specific binding and hydrophobic interactions were blocked by 1 h incubation at room temperature in 0.5% cold water fish skin gelatine (Sigma-Aldrich G7041) and 0.5% bovine serum albumin (Sigma-Aldrich A2153) in TBS pH 7.4 containing 0.05% tween 20 (Sigma-Aldrich P9416). Incubation of primary antibodies followed, with mouse anti vimentin (1:1000, ThermoFisher MA5-11883) and rabbit anti γ-tubulin (1:1000, Sigma-Aldrich T5192) in blocking solution for 48-h at 4°C. Sections were washed in TBS-tween and then incubated with the secondary antibody mix (goat anti-mouse Alexa Fluor 647 Abcam ab150115, Donkey anti-rabbit Alexa Fluor 488 ab150073) for 2 h at room temperature, followed by repeated rinses with PBS pH 7.4 and 1 min of treatment with TrueBlack lipofuscin autofluorescence quencher (Biotium 23007). The quencher was washed off with PBS pH 7.4 followed by counterstain for 10 min with Hoechst 33342 solution (1 μg/mL, ThermoFisher 62249) in PBS pH 7.4. Slides were mounted in 90% glycerol in PBS pH7.4 containing 2.5% Dabco 33-LV reagent (Sigma-Aldrich 290734), cover-slipped and sealed with nail polish. Sections were imaged using a Zeiss LSM 780 confocal microscope. Regions were selected on basis of section morphology to correspond to bregma -2.3 to bregma -2.9 in golden hamster brain atlas.[67] An overview image was taken at x10 objective using the counterstain followed by a 27 slice (10.18 μm thickness total) z stack with x63 magnification objective at either 400-600 μm distance from the median eminence outer boarder, to correspond to the alpha tanycyte region, or at the area by the 3rd ventricle floor (Median eminence), corresponding to the beta tanycyte region (Figure S2A). The capture settings with x63 objective were; ExHoechst: 405 nm, EmHoechst: 410-483 nm, ExAF488: 488nm, EmAF488: 514-630 nm, ExAF647: 633 nm, EmAF647:638-755 nm.

Six LP- and six SP-gestated animals were included in the analysis. Zeiss zen software was used to create maximum intensity projections from the z stack. The images were exported into QuPath for analysis. The area around the ventricle wall was selected for analysis, an intensity threshold of 20 and a size threshold of 260nm (average size of a basal body) was used to identify and count basal bodies. The number of identified basal bodies was normalized by the length of the ventricle included in the analysis to give the number of basal bodies per millimeter (mm).

Third ventricle face whole mounts for cilia

Three LP- and Three SP- gestated animals PEG embedded brains were dewaxed overnight in PBS pH 7.4 at room temperature with gentle shaking. In brief, under a stereoscope the wall of the 3rd ventricle was dissected out in PBS pH 7.4 using a scalpel and tweezers. Making a sagittal cut with a scalpel, an approximate 500 μm section containing the 3rd ventricle wall was then separated from the remaining hemisphere and stored in 12-well plate in PBS pH 7.4.

Antigen retrieval was performed with a 95°C trisodium citrate bath pH 6.0 for 1 h and left to cool for 1 h to room temperature before permeabilization for 10 min using PBS pH7.4 containing 0.2% Triton X-100 (Sigma-Aldrich T8787) and 0.05% Tween 20. The sections were blocked as described above. Primary incubation in blocking solution was done with a mix of mouse anti α-tubulin (1:1000 Sigma-Aldrich T6793) and rabbit anti γ-tubulin (1:500, Sigma-Aldrich T5192) at 4°C with gentle shaking. The sections were washed four times 20 min with gentle shaking in PBS pH 7.4 containing 0.05% tween 20. To minimize staining α-tubulin inside the cell, secondary antibodies were incubated for 1 h with 1:500 Goat Anti-Mouse Brilliant Violet 421 (Jackson Immuno research 115-675-166) and 1:500 goat anti rabbit Alexa flour 647 (Abcam ab150115) in blocking solution then washed again four time 20 min in PBS 0.05% tween 20 with gentle shaking. Sections were counterstained for 10 min with 1 μM SYTOX green (Thermo Fisher S7020) followed by three times 10 min washes before storage in PBS pH7.4 until imaging.

The sections were imaged on a Zeiss LSM800 confocal microscope by placing the sections ventricle side down in a Mattek dish (Mattek P35G-1.5-14-C) and fixed in place with a small circle of Twinsil (Picodent #13001000). A drop of antifade mounting medium and a coverslip were added to prevent section from drying out during imaging. Using the counterstain, an overview image was created by tiling 3-4 images containing 3-4 z-positions. Regions for high magnification were selected between 400 and 600 μm distance dorsally from the Median Eminence outer border (alpha tanycyte region) and 0-400 μm anteriorly from the most dorsal point of the pars tuberalis (beta tanycyte region) (Figure S2B). A 40 × 40 μm area was imaged with a x63 objective by taking a z stack consisting of 55-60 slices, starting above the ciliated wall, and ending 8-10 μm into the tissue. Capture settings with x63 objective used was ExBV421: 465 nm, EmBV421: 400-530 nm, ExSYTOXG: 504nm, EmSYTOXG: 517-565nm, ExAF647: 633 nm, EmAF647:450-700 nm.

The images were visualized using Zeiss Zen software and maximum intensity projections were created. The same display settings were applied to all images for each color channel. Representative images from an LP and SP-gestated animal from the alpha tanycyte region are shown (Figure 2F).

PCNA & Ki67 staining

The slides were taken from 4°C and rinsed in distilled water. Antigen reactivation was performed by submerging the slides in Citrate buffer (0.1M sodium monophosphate, 0.1M citric acid, pH 6) and autoclaving them. After cooling for 30 min at room temperature, slides were washed twice for 5 min in Tris buffer 0.1M (TB) and once in TB with 0.3% Triton X (TBX). Endogenous peroxidase expression was blocked with TB containing 0.3% H2O2 for 30 min (1.5% for 15 min for Ki67). After rinsing in TB and TBX, saturation of non-specific binding sites was performed by incubation in 5% normal horse serum (NHS; Vector Labs., Burlingame, CA, USA) in TBX for 1h. Incubation with primary antibodies took place overnight at room temperature. All antibodies were diluted in TBX, 2% NHS. The following primary antibodies were used: rabbit anti-Ki67 at 1:1000 (ab15580, Abcam) and monoclonal anti-PCNA made in mouse: PC10 at 1:10000 (ab29, Abcam). For negative controls, the slides were incubated in the same buffer in the absence of primary antibody. The next morning, slides were washed in TB and TBX. Then, slides were incubated for 1h using the secondary biotinylated rabbit universal antibody of the Vectastain Universal Elite ABC kit (Vector Labs.) at 1:400 in TBX, 2% NHS. Excess antibody was washed away with TB and TBX followed by 1 h incubation with the avidin-peroxidase complex (ABC) from the Universal Elite ABC kit (Vector Labs.) at 1:20 in TBX. The excess of ABC complex was washed away with TB and peroxidase activity was detected using niquel-3,3-diaminobenzidine (Ni-DAB) (0.5 mg/ml DAB (Sigma-Aldrich), 0.1M sodium acetate, 0.04% ammonium chloride, 2.5% nickel sulphate). After detection, slides were dehydrated in serial alcohols in distilled H2O (70%, 95%, 100%, and 100%), cleared in Histoclear (National diagnostics) and permanently mounted using Eukitt (Sigma-Aldrich).

Photographs were taken using a Zeiss Axioskop microscope fitted with a Zeiss Axiocam Icc1 camera (Carl Zeiss). Positive PCNA and Ki67 cell numbers were evaluated in ependymal layer up to 600μm from the base of the ventricle wall using Qupath. ImageJ was used to invert the PCNA images to aid visualization (Figure 3C).

QUANTIFICATION AND STATISTICAL ANALYSIS

The differential gene expression analysis was done using Rstudio, and the package EdgeR.[56] Three samples failed library construction and one sample from the SPIP group was excluded from the RNA-seq analysis because it had low read counts therefore it was an outlier in the PCA analysis. The final RNA-seq analysis the numbers of animals for each group analysis were LP = 5, SP = 5, SPIP = 4 and LPIP = 6. Significance in this study was defined as a false discovery rate below 0.001.

Graphpad prism was used to analyze body weight and testis weight (6 per group). Details of the statistical test and significances are given in the figure legend. One-way ANOVA and a Tukey test for multiple comparisons was used. Significance for these data were defined as an adjusted p value less than 0.05.

Graphpad prism was also used to test for statistical differences in the cilia (6 per group), as there were only two groups in this analysis an unpaired t-test was used. Significance for these data were defined as an p value less than 0.05.

Graphpad prism was used for the statistics to assess the age and photoperiod effects on cell division markers (ki67 and PCNA), details are given in the legends. In all cases either a one-way or two-way ANOVA and a Tukey test for multiple comparisons was used. Significance for these data were defined as an adjusted p value less than 0.05.